

# Vertical velocity variance and skewness in clear and cloud-topped boundary layers as revealed by Doppler lidar

Robin J. Hogan,<sup>a\*</sup> Alan L. M. Grant,<sup>a</sup> Anthony J. Illingworth,<sup>a</sup>  
Guy N. Pearson<sup>b</sup> and Ewan J. O'Connor<sup>a</sup>

<sup>a</sup>Department of Meteorology, University of Reading, UK

<sup>b</sup>HALO Photonics, Leigh, UK

**ABSTRACT:** In this paper, observations by a ground-based vertically pointing Doppler lidar and sonic anemometer are used to investigate the diurnal evolution of boundary-layer turbulence in cloudless, cumulus and stratocumulus conditions. When turbulence is driven primarily by surface heating, such as in cloudless and cumulus-topped boundary layers, both the vertical velocity variance and skewness follow similar profiles, on average, to previous observational studies of turbulence in convective conditions, with a peak skewness of around 0.8 in the upper third of the mixed layer. When the turbulence is driven primarily by cloud-top radiative cooling, such as in the presence of nocturnal stratocumulus, it is found that the skewness is inverted in both sign and height: its minimum value of around  $-0.9$  occurs in the lower third of the mixed layer. The profile of variance is consistent with a cloud-top cooling rate of around  $30 \text{ W m}^{-2}$ . This is also consistent with the evolution of the thermodynamic profile and the rate of growth of the mixed layer into the stable nocturnal boundary layer from above. In conditions where surface heating occurs simultaneously with cloud-top cooling, the skewness is found to be useful for diagnosing the source of the turbulence, suggesting that long-term Doppler lidar observations would be valuable for evaluating boundary-layer parametrization schemes. Copyright © 2009 Royal Meteorological Society

KEY WORDS decoupled boundary layer; stratocumulus

Received 29 June 2008; Revised 26 February 2009; Accepted 2 March 2009

## 1. Introduction

Numerous previous studies have used mixed-layer scaling to characterize the statistics of turbulence in the daytime cloudless planetary boundary layer observed by aircraft (e.g. Lenschow *et al.*, 1980; Young, 1988). It has been found that when normalized by the square of the convective velocity scale,  $w_*^2$ , the vertical velocity variance is a universal function of normalized height,  $z/h$ , where  $h$  is the depth of the mixed layer. Likewise, vertical velocity skewness, given by

$$s = \frac{\overline{w'^3}}{w_*^3} \frac{\overline{w'^2}}{w_*^2}^{3/2}, \quad (1)$$

where  $w'$  is the fluctuation from the mean vertical wind, tends to have a characteristic shape as a function of  $z/h$  in convective conditions (LeMone, 1990), being positive throughout the layer and increasing with height. This expresses the fact that in a surface-heating-driven boundary layer, the updraughts tend to be narrower and more intense than the broader, weaker downdraughts.

In cloud-topped boundary layers, turbulence is often driven by cloud-top long-wave radiative cooling and can

be thought of as an 'upside-down' version of surface-driven turbulence, this time with negative skewness indicating the downdraughts to be typically narrower and more intense than the updraughts. Moyer and Young (1991) presented aircraft-derived turbulence statistics in cloud-topped marine boundary layers. In a case near sunset (their flight C), when cloud-top radiative and evaporative cooling dominated over surface heating and negatively buoyant plumes generated at cloud top were able to penetrate down to the surface, they found negative skewness at almost all heights with a minimum value of  $-0.6$  in the middle of the mixed layer. However, the turbulence in cloudy boundary layers can often be more complex when both surface heating and cloud-top cooling are present. Moyer and Young (1991) also presented a cloudy daytime case (their flight B), in which cloud-top cooling maintained a negative skewness in the upper part of the boundary layer, but in the lower part the eddies were primarily driven by surface heating and the skewness was positive. Albrecht *et al.* (1995) presented cloud-radar observations of a stratocumulus-topped marine boundary layer that was predominantly stable. In the uppermost 250 m of the cloud, they reported a vertical velocity variance of  $0.1 \text{ m}^2 \text{ s}^{-2}$  and a skewness as low as  $-0.8$ , but in the lower part of the cloud the variance was much lower and the skewness was close to zero.

\*Correspondence to: Dr Robin Hogan, Department of Meteorology, University of Reading, Earley Gate, PO Box 243, Reading RG6 6BB, UK.  
E-mail: r.j.hogan@reading.ac.uk

So why does the sign of the skewness indicate whether turbulence is driven by surface heating or cloud-top cooling? The reason is that in the equation for the evolution of  $\overline{w'^2}$ , the triple correlation  $\overline{w'^3}$  represents the vertical transport of  $\overline{w'^2}$  by the turbulence itself (e.g. Bougeault and André, 1986). It plays the same role in the equation for the evolution of turbulent kinetic energy (TKE). Hence when  $\overline{w'^3}$  (and therefore skewness) is positive, both  $\overline{w'^2}$  and TKE are being transported upwards. In a well-mixed boundary layer heated from below, the dominant source term for  $\overline{w'^2}$  and TKE above the surface layer is buoyancy generation, which is proportional to sensible heat flux and is maximum at the surface, decreasing linearly towards the top of the mixed layer (Garratt, 1992). The consequence is that the ascending parts of the larger eddies tend to be more turbulent than the descending parts, such that there is a net transport of TKE upwards and  $\overline{w'^3}$  is positive.

By contrast, in a well-mixed layer cooled from above, the buoyancy generation of TKE *increases* with height to a maximum at the top of the layer (Nicholls, 1984). Therefore the turbulent transport of TKE is downwards and  $\overline{w'^3}$  is negative. Note that TKE is dissipated into heat at a rate that is more constant with height than the generation by buoyancy. Hence the combination of variance and skewness can be used to reveal the intensity and origin of the turbulence in complex boundary-layer situations.

In this paper we demonstrate how a continuously operating, vertically pointing Doppler lidar may be used to obtain these quantities on a routine basis and therefore map out the diurnal evolution of boundary-layer characteristics. Lidar has the advantage over cloud radar that it detects aerosol particles and so measures vertical velocity throughout the boundary layer, not just in the cloud. Furthermore, cloud radar returns from stratocumulus are often dominated by drizzle drops that are not tracers of the air motion (e.g. O'Connor *et al.*, 2005). One limitation of lidar is that it cannot penetrate optically thick cloud, and so cannot always see to the top of the boundary layer in cases of thick stratocumulus. In this paper we consider only cases of thin stratocumulus.

The paper is organised as follows. In section 2 the quantities derived from the Doppler lidar and the sonic anemometer are described. In section 3, the turbulence statistics from cloudless and cumulus-topped boundary layers are presented and compared to relationships from the literature, giving us confidence in the inferences from the lidar. Then in section 4, a more complex case is presented in which turbulence is driven at various times from both the surface and from the stratocumulus at the top of the boundary layer.

## 2. Method

The observations in this paper were made at the Chilbolton Observatory in southern England (51° 09'N, 01° 26'W). Since September 2006, a 1.5  $\mu\text{m}$  heterodyne

Doppler lidar has been operated nearly continuously in a vertically pointing configuration, a very similar instrument to that used by Bozier *et al.* (2007). The lidar records profiles of attenuated backscatter coefficient,  $\beta$ , and Doppler velocity,  $w$ , and is sensitive to both cloud and aerosol. Both are assumed to be tracers of the wind field. The lidar has a range-gate spacing of 36 m and a nominal time resolution of  $\Delta t = 32$  s. The accuracy of the Doppler velocity is around 3–4  $\text{cm s}^{-1}$  at high signal-to-noise ratios (Pearson *et al.*, 2009).

We characterize the intensity of the turbulence by the variance of the vertical velocity,  $\sigma_w^2$ , over an hour-long period and three range-gates in the vertical. Three gates are found to give a good balance between reducing error in the variance estimates and maintaining a useful vertical resolution. The measured velocity every pixel may be decomposed into the sum of the mean over the hour,  $\overline{w}$ , and the fluctuation from the mean,  $w'$ . The variance is given by

$$\sigma_w^2 = \overline{w'^2} + \epsilon, \quad (2)$$

where  $\epsilon$  is the contribution from small scales unsampled by the 32 s temporal resolution. The  $\epsilon$  term is estimated for each hour-long period as follows. A Fourier Transform is performed on the time series of  $w$  to obtain the power spectrum at each of the three range-gates, which are then averaged to obtain a single power spectrum  $S_w(f)$ , where  $f$  is the frequency. A minus-five-thirds power law of the form  $S_w(f) = S_0 f^{-5/3}$  is fitted to the highest third of the frequency domain, i.e. between frequencies of  $1/3\Delta t$  and the Nyquist frequency of  $1/2\Delta t$ . This is achieved simply taking  $S_0$  to be the average of  $S_w(f) f^{5/3}$  over this frequency range. This power law is then extrapolated out to an infinite frequency, corresponding to time-scales between 0 and  $2\Delta t$ , and  $\epsilon$  is calculated as the integral under the extrapolated region:

$$\epsilon = S_0 \int_{1/2\Delta t}^{\infty} f^{-5/3} df = \frac{2}{3} S_0 \Delta t^{2/3}. \quad (3)$$

Thus we are assuming that motions with a period shorter than  $2\Delta t/3$  are within the inertial subrange.

Figure 1 illustrates this process applied to lidar measurements in a cumulus-topped convective boundary layer on 11 July 2007. (The somewhat steeper slope than  $-2/3$  for frequencies in the range 5–9 mHz is believed to be simply a symptom of noise in the lidar measurements.) In practice it is found that in convective conditions this procedure increases the variance by 0–30% (hence increasing the standard deviation,  $\sigma_w$ , by 0–15%), while in stable conditions, when most of the variance is contained in smaller eddies, the typical increase is closer to 70% (30% in terms of standard deviation). Note that for typical horizontal wind speeds in the boundary layer during the cases in this paper, a sampling time of 32 s corresponds to a horizontal scale of 100–350 m. We would therefore expect the error associated with this procedure to be small (less than 10% in  $\sigma_w^2$ ) in convective conditions, but

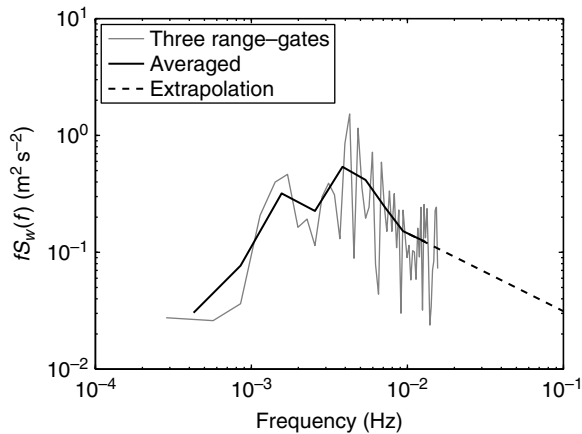


Figure 1. Vertical velocity power spectrum,  $S_w(f)$ , multiplied by frequency  $f$ , for the lidar observations between 14 and 15 UTC on 11 July 2007 at a height of around 600 m. The thin grey line shows the average of the spectra from three adjacent range-gates, while the black solid line shows the same but after further averaging in frequency space. The dashed black line shows a  $-5/3$  power law ( $-2/3$  for  $fS_w(f)$ ) fitted to the high-frequency end of the measured power spectrum and extrapolated to estimate the variance associated with the unsampled higher-frequency fluctuations. In this case the raw vertical velocity standard deviation is  $\overline{w^2}^{1/2} = 0.94 \text{ m s}^{-1}$ , but after including the high-frequency contribution is increased to  $\sigma_w = 1.02 \text{ m s}^{-1}$ .

considerably larger in stable conditions due to the possibility that the spectra do not encompass any of the inertial subrange. In this paper the variances are only used quantitatively in convective conditions, but if in a future paper the variances in stable conditions were to be studied, then more rapid sampling than 32 s would be required.

The skewness of the vertical velocity is estimated using (1) and is again calculated from each hour-long period and three range-gates. Unlike with variance, no attempt is made to account for the unsampled fluctuations in the calculation of the skewness. It is implicitly assumed that the dominant contribution to skewness tends to be from the largest scales of motion present within a convectively mixed layer. This is valid since the asymmetry between the width and intensity of updraughts and downdraughts is most apparent in the large boundary-layer-scale eddies (Garratt, 1992). The good agreement with other studies of the shape and magnitude of the skewness profile, to be presented in the next section, also provides support for this assumption, although it would be desirable to test it rigorously using high-frequency aircraft data. In section 4, cospectra are used to examine the scale of the eddies that contribute to  $\overline{w^3}$ .

Finally, the lidar is used to estimate the boundary-layer depth,  $h$ , for comparison with the other measurements. In the days considered in this paper, the aerosols provided a very clear indication of the location of the boundary-layer top, with no aerosols detectable above it. Therefore in each 32 s profile, the height of the highest-altitude aerosol echo in the lowest 2 km of the atmosphere was recorded. The boundary-layer top was defined as the median height over the hour-long period. During the first few hours of daylight each day, this method will identify the height of the so-called 'residual layer', i.e. the remnants of the

previous day's convective boundary layer, rather than the new convective boundary layer. Therefore, we are careful to use  $h$  estimated by this method only when the new convective boundary layer has fully penetrated the residual layer, which is easy to identify subjectively from backscatter images. Therefore it is not necessary to implement an advanced boundary-layer top identification scheme (e.g. Davis *et al.*, 2000; Davies *et al.*, 2007).

Chilbolton is equipped with a sonic anemometer and an open-path gas analyzer mounted at a height of 5 m. These instruments simultaneously measure sonic temperature, the three components of wind, and the concentrations of water vapour and carbon dioxide, all at a rate of 20 Hz. Standard eddy-correlation techniques are used to estimate sensible heat flux  $H = \rho C_p \overline{w'T'}$  averaged over an hour, where  $\rho$  is the density of the air,  $C_p$  is the specific heat of dry air and  $T'$  is the fluctuation of temperature from its mean value. The covariance is calculated over the same hour-long periods as used in analysing the Doppler lidar data, and a linear trend is removed from both  $w$  and  $T$  before calculating the covariance. Latent heat flux is defined as  $\lambda \overline{w'\rho'_v}$ , where  $\lambda$  is the latent heat of vaporization of water,  $\rho'_v$  is the water vapour density and again the mean is taken over an hour.

In convective conditions, the surface flux measurements, together with the depth of the boundary layer, may be used to estimate the convective velocity scale defined as

$$w_* = \left( \frac{g}{T_v} \overline{w'T'_v} h \right)^{1/3}, \quad (4)$$

where  $g$  is the acceleration due to gravity and  $T_v$  is the virtual temperature. Note that  $w_*$  has previously been estimated using Doppler lidar by Davies *et al.* (2004).

### 3. Clear-sky and cumulus-topped daytime boundary layers

Figure 2 shows the observations from a cloudless boundary layer on 22 May 2007 (except for thin liquid clouds between 0000 and 0300 UTC). The difference between stable and convective conditions is striking in all variables. Before around 0800 UTC, the stratification of the boundary layer is evident from the layered structures in the aerosol backscatter in Figure 2(a). The vertical velocity standard deviation,  $\sigma_w$ , is less than around  $0.2 \text{ m s}^{-1}$ , and there is no significant signal in the skewness. During the morning the growth of the convective boundary layer is evident in Figure 2(a), with the laminar structures being replaced by vertically uniform backscatter, indicating that the aerosol was well mixed. The peak surface sensible heat flux of around  $140 \text{ W m}^{-2}$  corresponded to a maximum in  $\sigma_w$  of around  $1.2 \text{ m s}^{-1}$ . Figure 2(d) reveals this turbulent activity to be associated with a positive skewness with a peak value of around 0.8.

Figure 3 shows the same as Figure 2 but for a shallow-cumulus-topped boundary layer on 11 July 2007. Again, the surface-heating-driven daytime turbulence is associated with  $\sigma_w$  of up to  $1.2 \text{ m s}^{-1}$  and skewness of around

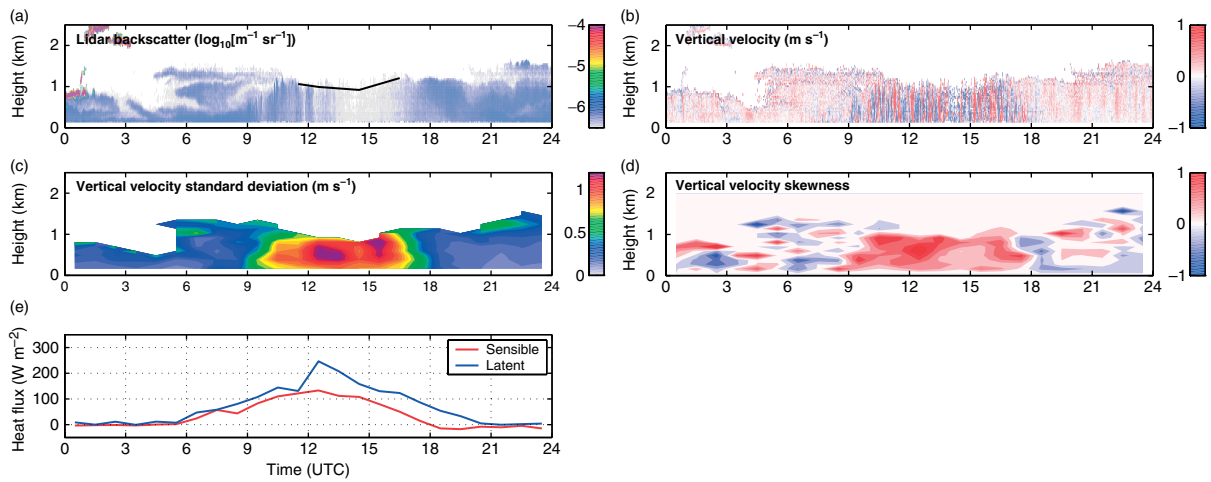


Figure 2. Observations taken on 22 May 2007: (a) attenuated lidar backscatter coefficient with the daytime-derived 1-hour mean boundary-layer top shown by the black line, (b) vertical velocity, (c) 1-hour standard deviation of vertical velocity  $\sigma_w$ , (d) skewness of vertical velocity, and (e) surface sensible and latent heat fluxes.

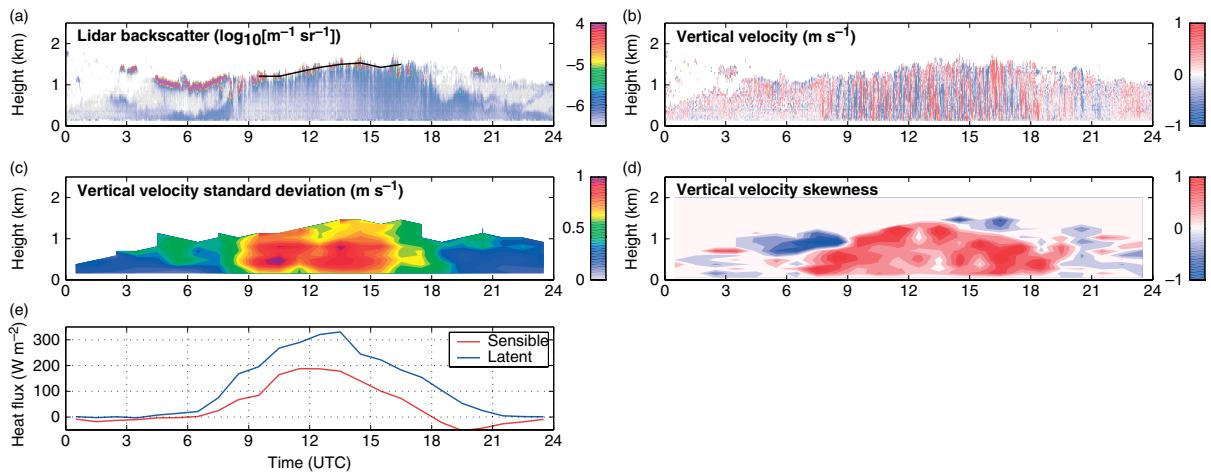


Figure 3. As Figure 2, but for 11 July 2007.

0.8. Regular cloud-camera images from Chilbolton confirm that only cumulus was present after 0900 UTC, but earlier in the morning a more continuous sheet of stratocumulus was detected by the lidar at a height of 1 km. An interesting feature of Figure 3(d) is that this stratocumulus was associated with significantly negative skewness. This is a tell-tale sign of turbulence driven by radiative cooling at the top of the layer, rather than by

sensible heating at the base of the layer, a phenomenon that is explored in more detail in section 4.

We now compare the variance and skewness observations to those in the literature. Figure 5(a) shows the variance,  $\sigma_w^2$ , normalized by  $w_*^2$ , for two cloudless and four shallow-cumulus-topped boundary layers. This ratio is plotted as a function of height normalized by the depth of the boundary layer as estimated by the lidar,  $h$ . As

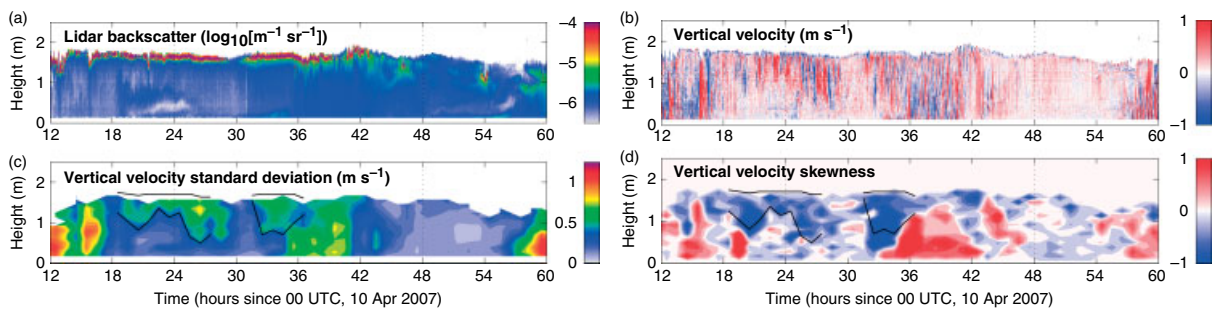


Figure 4. As Figures 2(a–d) but for 48 hours of observations from 12 UTC on 10 April 2007. The solid black lines in (c) and (d) indicate the boundaries of the elevated mixed layer discussed in the text.

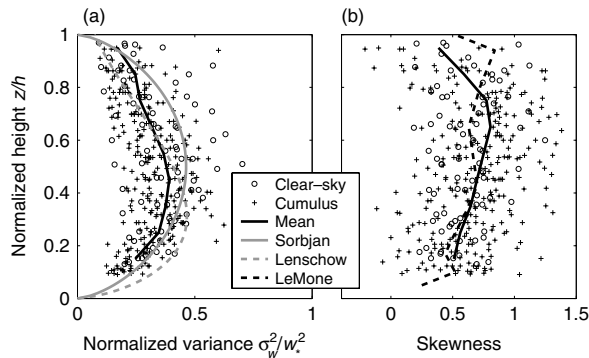


Figure 5. (a) Normalized variance of the vertical velocity as a function of the fraction of the depth of the boundary layer. The circles indicate 1-hour/108-m Doppler lidar observations taken in cloudless convective boundary layers on 22 May (shown in Figure 2) and 25 August 2007. The plus-signs show the same but for four shallow-cumulus days: 7 July, 11 July (depicted in Figure 3), 24 July and 27 August 2007. The black line shows the mean of all these points. The grey solid line shows the fit of Sorbjan (1989) to observations in cloudless boundary layers, while the grey dashed lines show the fit of Lenschow *et al.* (1980). (b) Skewness from the same Doppler lidar observations in (a) with the mean to these data shown by the solid line. The dashed line shows the mean to observations by LeMone (1990).

discussed in section 2, we only used periods when a new convective mixed layer had penetrated to the full depth of the aerosol-filled boundary layer, and hence when  $h$  was reliable; this was typically between 1000 and 1600 UTC each day. In these situations, the correction for unsampled eddies described in 2 had the smallest fractional effect on  $\sigma_w^2$  (less than 30%), and hence the results here should be accurate to around 10%. The thick black line depicts the mean of the measurements, and shows  $\sigma_w^2/w_*^2$  to peak at around 0.4 at a height of around 40% of the depth of the boundary layer. Two analytic profiles are shown for comparison, the symmetric profile from Sorbjan (1989):

$$\frac{\sigma_w^2}{w_*^2} = 1.17 \left[ \frac{z}{h} \left( 1 - \frac{z}{h} \right) \right]^{2/3}, \quad (5)$$

and the asymmetric profile from the aircraft measurements of Lenschow *et al.* (1980):

$$\frac{\sigma_w^2}{w_*^2} = 1.8 \left( \frac{z}{h} \right)^{2/3} \left( 1 - 0.8 \frac{z}{h} \right)^2. \quad (6)$$

The mean profile from this study agrees with the analytic profiles about as well as the analytic profiles agree with each other, and certainly lies within the gamut of relationships that were compared by Young (1988). This supports the validity of extending the spectrum to account for small unresolved scales as described in section 2, at least in convective conditions. Our observations exhibit a peak in variance in the lower half of the mixed layer, although the profile is seemingly not as asymmetric as that of Lenschow *et al.* (1980).

Figure 5(b) depicts the corresponding skewness profiles, along with the observed profiles of LeMone (1990) measured by aircraft. The agreement is very good in magnitude, with the skewness generally increasing with height. This agreement with previous work gives us

confidence in using the Doppler lidar to investigate other types of boundary layer than the well-studied convective daytime boundary layer.

In neither the variance nor the skewness profiles is there a significant difference between cloudless and cumulus-topped boundary layers, suggesting that shallow cumulus usually play a minor role in the turbulence budget of the boundary layer. A similar conclusion was reached by Nicholls and LeMone (1980) regarding the effect of cumulus on the profile of virtual heat flux. The one exception is in the upper 10% of cumulus-topped boundary layers, where skewness occasionally becomes negative. This is also observed after 1400 UTC in Figure 3(d), and is presumably because the associated radiative cooling is sufficient to generate downdrafts that penetrate a short distance into the boundary layer from above.

#### 4. Stratocumulus-topped boundary layers

We now consider a case of nocturnal stratocumulus that was observed on the night of 10–11 April 2007. No surface flux measurements were available at this time. Figure 4 shows the lidar measurements over a 48-hour period, with the stratocumulus evident as the layer of high backscatter at an altitude of 1.8 km between 1200 UTC on 10 April and around 1800 UTC on 11 April. A turbulent mixed layer is clearly evident in the upper half of the boundary layer on the night of 10 April, with  $\sigma_w$  reaching a maximum of around  $0.6 \text{ m s}^{-1}$ . This was clearly driven from cloud top as it is isolated from the surface by a non-turbulent layer, and associated with negative skewness. Furthermore, the mixed layer appears to have been deepening with time, progressively encroaching into the stable boundary layer below it. This picture is confirmed at 0600 UTC on 11 April (30 hours in the figure) when a break in the cloud coincided with a rapid drop in the intensity of the turbulence as diagnosed by  $\sigma_w$ .

One hour later the cloud and associated turbulence returned. The resulting mixed layer can be seen to have deepened and the associated negative skewness nearly reached down to ground level at around 0800 UTC. After this time the situation became even more interesting as surface heating led to the growth of a new convective boundary layer. Figure 4(d) shows a sharp interface between the positive skewness associated with the surface-driven convection and the negative skewness of the cloud-top-driven convection. Over time the interface rose, presumably indicating that the surface sensible heat flux was larger than the cloud-top radiative cooling, and by around 1600 UTC on 11 April, the surface-driven turbulence almost filled the entire boundary layer. By around 2000 UTC the cloud had dissipated and the surface heating ceased, resulting in virtually zero turbulence until surface heating recommenced the following day.

The detailed vertical motions at the interface between the surface- and cloud-top-driven turbulence are depicted in Figure 6, with the black line indicating the zero-skewness contour. The tendency is clearly visible for the

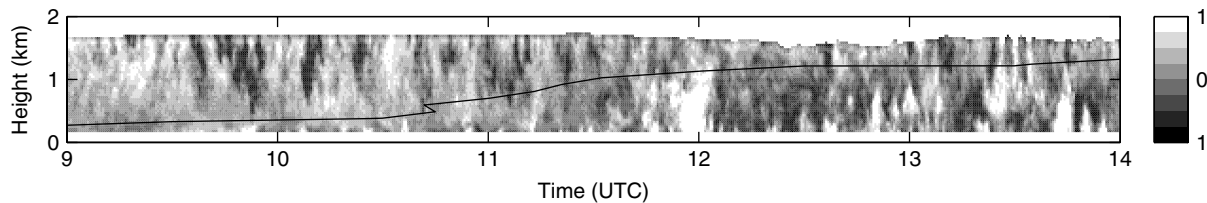


Figure 6. Vertical velocity on 11 April 2007, corresponding to the central period of Figure 4(b) (but note that the time axis is now since 0000 UTC on 11 April). The black line is the zero-skewness contour.

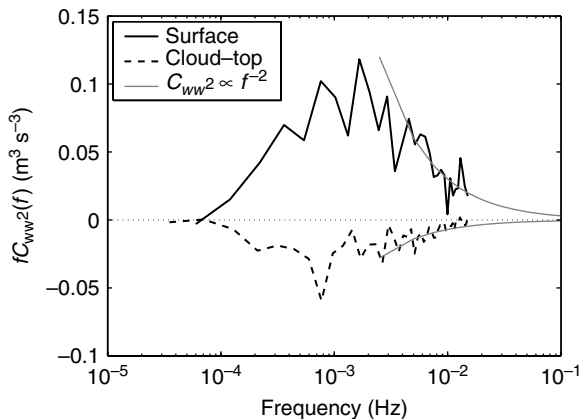


Figure 7. Skewness cospectra,  $C_{ww^2}(f)$ , for (black solid line) surface-driven turbulence at an altitude of 500 m between 1100 and 1800 UTC, and (black dashed line) cloud-top-driven turbulence at 1100 m between 0000 and 1200 UTC, both on 11 April 2007. Note that the cospectra have been multiplied by frequency  $f$  such that the area under the curve plotted versus frequency in logarithmic space is proportional to the contribution to  $\overline{w'^3}$ . To reduce noise, the cospectra have been averaged over three adjacent range-gates and in frequency. The thin grey lines show the theoretical dependence of the cospectrum on the inverse-square of frequency at small scales (Hunt *et al.*, 1988).

updraughts to be narrower and more intense below the line while the same is true of the downdraughts above the line. Despite the sharp difference in skewness, there are many examples of both ascending and descending plumes passing through this interface.

To characterize the scales of motion that are contributing to skewness, we can use cospectra. Following Hunt *et al.* (1988), the cospectrum of  $w'$  and  $w'^2$  we denote as  $C_{ww^2}$ , and is calculated as the complex conjugate of the Fourier Transform of  $w'$  multiplied by the Fourier Transform of  $w'^2$ . This then satisfies the relationship

$$\overline{w'^3} = \int_0^\infty C_{ww^2}(f) df. \quad (7)$$

Therefore,  $C_{ww^2}(f)$  can be treated as the spectral decomposition of  $\overline{w'^3}$ , in the same way that an ordinary power spectrum expresses the spectral decomposition of  $\overline{w'^2}$ . Figure 7 depicts the cospectra of time-series of Doppler lidar velocities measured in surface-driven and cloud-top-driven turbulence on 11 April 2007, with corresponding skewness values of +1.27 and -0.78, respectively. The cospectra are of opposite sign, simply reflecting the sign of  $\overline{w'^3}$  and the skewness. The eddies that contribute most to the skewness appear to have a

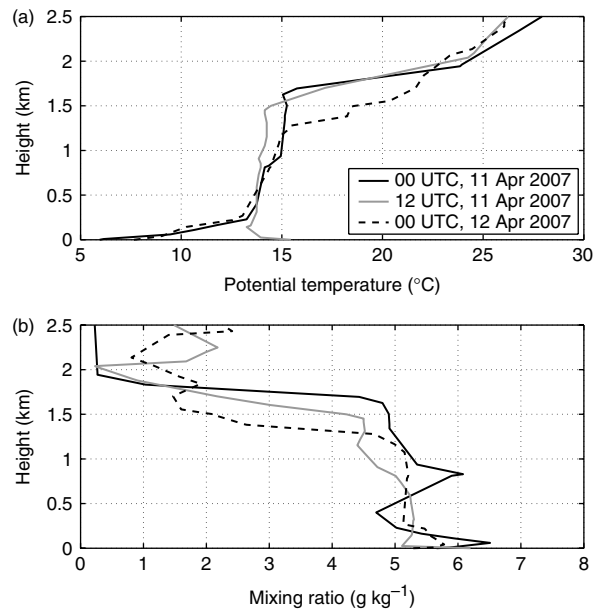


Figure 8. Radiosonde profiles from Herstmonceux of potential temperature and water vapour mixing ratio at 12-hour intervals starting at 0000 UTC on 11 April 2007, corresponding to hours 24, 36 and 48 on the time axis of Figure 4. The first two profiles almost reached saturation at the top of the mixed layer at around 1.6 km.

time-scale of around 15 minutes, which corresponds to the turnover time of large boundary-layer-scale eddies. At smaller scales (higher frequencies), the decrease of the cospectra with frequency is consistent with the  $f^{-2}$  dependence predicted by the scaling arguments of Hunt *et al.* (1988). Therefore, the small eddies that are unresolved by the 32 s resolution of the Doppler lidar contribute less to  $\overline{w'^3}$  than they do to the variance  $\overline{w'^2}$ , for which the power law dependence is  $f^{-5/3}$ .

It is illuminating to study the 12-hourly radiosonde ascents from Herstmonceux, shown in Figure 8. Herstmonceux is located 125 km to the east of Chilbolton and during the period of these observations the horizontal wind was weak (around  $2.5 \text{ m s}^{-1}$  at the altitude of the cloud) and generally from the east. Potential temperature,  $\theta$ , and water vapour mixing ratio are shown in Figures 8(a) and (b), respectively. Note that in none of these ascents did the air quite reach saturation, confirming that the stratocumulus cloud observed at Chilbolton was thin. The solid black line shows the ascent at 0000 UTC on 11 April. A well-mixed layer is clearly apparent with  $\theta$  constant at  $15^\circ\text{C}$  between 0.9 and 1.5 km. This is topped by a slightly superadiabatic layer just beneath the main  $9^\circ\text{C}$  capping inversion. The superadiabatic layer is a signature

of the cloud-top radiative cooling, and will have generated negatively buoyant plumes that descended into the well-mixed layer, maintaining and deepening it. Immediately beneath the well-mixed layer is a  $1^\circ\text{C}$  inversion and beneath that the atmosphere is weakly stable down to the nocturnal surface inversion in the lowest 200 m.

The simplest way to understand this profile is to turn it upside down: the similarity to a convective daytime boundary-layer profile is then obvious. Thus the superadiabatic layer in this case plays the same role as the unstable surface layer of a daytime profile, while the inversion at 0.9 km acts in the same way as the capping inversion of a daytime profile. Clearly the temperature gradients associated with both the superadiabatic layer and the 0.9 km inversion are much weaker than a typical daytime profile, which is presumably due to the weaker magnitude of radiative cooling compared to the surface sensible heating in a typical daytime convective boundary layer.

The grey line in Figure 8(a) shows the thermodynamic profiles 12 hours later. The nocturnal surface inversion has been replaced by an unstable surface layer, above which is a more adiabatic layer up to 0.9 km. This is consistent with the positive skewness evident at 1200 UTC in Figure 4(d) indicating surface-driven convection underlying the continued cloud-top-driven convection in the upper layer. It can be seen that the upper mixed layer is around  $1^\circ\text{C}$  cooler than the previous profile, although still retains the weak superadiabatic layer at the top of the layer. Assuming that the difference between the two profiles is purely due to local diabatic effects rather than advective forcing, the reduction of thermal energy in the upper layer is calculated to be  $691\text{ kJ m}^{-2}$ . Over 12 hours, this implies a mean cooling rate of  $16.0\text{ W m}^{-2}$ . It can be seen in Figure 8(b) that the cooling of the upper layer was associated with a drying, possibly caused by the entrainment of dry air from above the main inversion. There is likely also to have been entrainment of potentially cooler air from below. If the same physics applies as in the surface-driven convective mixing, we would expect the entrainment heat flux at the base of the mixed layer to be around 25% of the imposed heat flux at cloud top (vanZanten *et al.*, 1999).

We next reconcile the turbulent statistics from the Doppler lidar with the picture of upside-down convection. It is first necessary to define the boundaries of the upper mixed layer. The top of the layer,  $h$ , is derived from the lidar backscatter profile as before. It should be noted that the highest pixel with non-zero backscatter was generally in cloud. It is known that liquid water clouds can cause rapid lidar extinction and the cloud top (and hence boundary-layer top) may not be detected (e.g. Hogan *et al.*, 2005). However, the fact that the radiosondes did not quite reach saturation implies that the clouds were very thin and hence we do not believe that this will lead to errors of more than 100 m. The height of the base of the mixed layer, or ‘transition layer’,  $z_t$ , is estimated from hour-averaged profiles of  $\sigma_w$  and skewness using the following empirical rules. If there is no height in the profile where skewness is greater than 0.25, then there is assumed to be no surface-driven

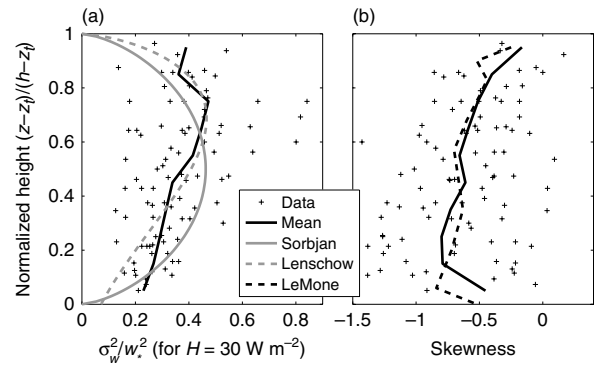


Figure 9. Similar to Figure 5, but for the elevated mixed layer bounded by the black lines in Figures 4(c) and (d), as a function of normalized height into the mixed layer, where  $z_t$  denotes the height of the base of the mixed layer and  $h$  the top of the mixed layer. (a) The plus signs show the 1-hour/108-m measurements of normalized variance, where  $w_*$  has been calculated assuming a heat flux into the layer of  $H = 30\text{ W m}^{-2}$ . Also shown are the mean of these points in normalized-height intervals of 0.1, and the analytic profiles from Sorbjan (1989) and Lenschow *et al.* (1980), the latter inverted in height. (b) The corresponding skewness profile and its mean. This is compared to the profile from LeMone (1990) shown in Figure 5(b), except that it has been inverted both in sign and in height.

convection and  $z_t$  is defined to be the lowest height for which  $\sigma_w$  exceeds  $0.35\text{ m s}^{-1}$ . If skewness does exceed 0.25 then  $z_t$  is the point above this where it drops below zero. The black lines in Figures 4(c) and (d) indicate where a cloud-top-driven mixed layer has been identified. Note that within this mixed layer, and in the ‘transition’ layer between surface-driven and cloud-top-driven turbulence, the correction for unresolved motions described in section 2 affected  $\sigma_w$  by less than 15%.

Figure 9(b) depicts the skewness profile as a function of normalized height into the layer. As before, there is considerable scatter of the individual points, but this time it is overwhelmingly negative and the mean profile clearly shows a decrease to the base of the layer. This profile is remarkably similar to the measured profile in a daytime convective boundary layer of LeMone (1990), *provided that her profile is inverted in both sign and height*. This confirms that cloud-top-driven convective mixing is very similar in character to surface-driven convection, but inverted.

The similarity in the skewness profile is actually more surprising than might be first supposed. Previous large-eddy simulations of surface-driven turbulence have tended to overestimate the skewness at the top of the layer, and one hypothesis that has been tested is that the difference is due to the upper boundary being treated as no-slip rather than free-slip as in the real atmosphere (Moeng and Rotunno, 1990). In the present case, the cooling at cloud top occurs at a free-slip boundary, unlike surface heating. Hence it is a little surprising that the skewness agrees with the inverted LeMone (1990) profile at the top of Figure 9(b), and indeed to the inverted results obtained by the lidar in surface-driven convection in Figure 5(b).

In the case of the variance of the vertical velocity, we cannot compare directly with characteristic profiles

of surface-driven turbulence because we do not have a measurement of the cloud-top heat flux, and hence the value of  $w_*$  to use to normalize the profile. However, given the agreement with the skewness profiles, we argue that it is possible to estimate the cloud-top heat flux based on its ability to produce a normalized variance profile that agrees, on average, with previous studies. Figure 9(a), shows the profile of normalized variance calculated assuming an equivalent cloud-top cooling rate of  $H = 30 \text{ W m}^{-2}$ , which was converted to a convective velocity scale. There is considerable scatter, partially due to the fact that the cooling rate will not have been exactly constant during the period, but this value of  $H$  results in the mean profile having approximately the same magnitude as the symmetric profile of Sorbjan (1989). However, there is a tendency for the variance to increase with height with the peak value occurring around 70% into the depth of the layer. This is opposite to the behaviour observed in Figure 5(a) for surface-driven convection in which the peak occurred in the lower half of the layer, yet it agrees well in shape with the inverted profile of Lenschow *et al.* (1980). Garratt (1992) showed that the variance profiles from the aircraft measurements of Nicholls (1989) in stratocumulus-topped marine boundary layers also matched the inverted profile of Lenschow *et al.* (1980).

Thus we have two estimates for the cloud-top cooling rate:  $16 \text{ W m}^{-2}$  from comparing two Hertmonceux radiosonde ascents and  $30 \text{ W m}^{-2}$  from the variance profile. There are numerous possible causes for the difference. Firstly, the cloud was not continuous for the entire 12-hour period between the two sondes, with a notable break in the cloud at around 0600 UTC on 11 April, indicating that the cooling of  $30 \text{ W m}^{-2}$  inferred from the variance profile would not have been acting all the time. Secondly, mixing of potentially warmer air from above and potentially colder air from below could have occurred simultaneously. Moreover, the cloud conditions were not necessarily exactly the same at Chilbolton and at Herstmonceux, and the cloud could have been more broken at Herstmonceux. Finally, although the wind was fairly weak, we cannot rule out the possibility of advection of warmer air from the east.

Finally in this section we attempt to estimate the growth of the 'upside-down' mixed-layer driven by cloud-top radiative cooling, using theory derived for the surface-driven mixed layer. Carson (1973) showed that in the absence of large-scale subsidence, the depth of a convective mixed layer growing into a stable profile with a potential temperature lapse rate of  $\gamma$  could be written as a function of time  $t$  as:

$$h(t) = 1.4 \left( \frac{2\overline{w'\theta'_{v0}t}}{\gamma} \right)^{1/2}, \quad (8)$$

where the surface virtual potential temperature flux,  $\overline{w'\theta'_{v0}}$  is assumed constant with time. The factor of 1.4 accounts for the presence of an entrainment heat flux into the boundary layer at its top to have a magnitude

of around 25% of the surface sensible heat flux (e.g. vanZanten *et al.*, 1999). This formula may be applied in a straightforward fashion to an elevated mixed layer with a fixed cloud-top cooling. The estimated cloud-top heat flux of  $30 \text{ W m}^{-2}$  corresponds to a virtual potential temperature flux of around  $0.03 \text{ K m s}^{-1}$  (neglecting the difference of less than 5% between heat flux and virtual heat flux, which is justified given that the figure of  $30 \text{ W m}^{-2}$  is not accurate to better than 10%). The stable lapse rate at 0000 UTC in Figure 8(a) below the weak inversion at 0.9 km was around  $\gamma = 1 \text{ K km}^{-1}$ , which lies within the  $0.8\text{--}3 \text{ K km}^{-1}$  range found by Grant (1997). These values predict a mixed-layer depth of around 1.1 km after 3 hours, which is approximately what is observed in the 24–27 hour and 31–34 hour growth periods in Figure 4(c).

## 5. Conclusions

In this paper the potential of a continuously operating, vertically pointing Doppler lidar to monitor the properties of boundary-layer turbulence has been demonstrated. In particular, the combination of vertical velocity variance and skewness allows one to distinguish between laminar flow and turbulence driven by both surface heating and cloud-top cooling. After demonstrating that the statistics of well-mixed daytime boundary layers driven by surface heating agree with those previously reported by aircraft observations, a more complex cloudy boundary layer was analyzed. This case was particularly interesting because the cloud layer remained very thin, and so acted purely as a sink of heat at the top of the boundary layer, without the effects of condensation on buoyancy generation becoming important. We found that, in almost all respects, cloud-top-driven turbulence behaves as an upside-down version of surface-driven turbulence. In particular:

- The mean skewness profile, when plotted against the normalized depth into the mixed layer, was inverted in both sign and height, but otherwise strikingly similar to the observations of LeMone (1990) in surface-driven turbulence;
- The variance profile, when suitably normalized, was an inverted version of its surface-driven counterpart, with the peak value lying on average around 30% into the mixed layer from the top;
- The growth of the mixed layer was predicted well by the model of Carson (1973), originally devised for surface-driven convection.

Potentially such observations could be used to evaluate boundary-layer parametrizations in numerical forecast models, in a similar manner to the use of long-term cloud radar observations to evaluate cloud forecasts (Illingworth *et al.*, 2007). In particular, the scheme of Lock *et al.* (2000) categorizes boundary-layer profiles into one of six categories, five of which were identified in this study. (The only one not identified was decoupled stratocumulus over cumulus.) However, if stable layers are to be studied quantitatively, then higher temporal resolution would be

required than the 32 s used here in order to resolve the important eddies.

### Acknowledgements

The 1.5  $\mu\text{m}$  Doppler lidar was acquired with NERC grant NE/C513569/1. The sonic anemometer and open-path gas analyzer were acquired with NERC grant NE/D005205/1. The instruments at Chilbolton are operated and maintained by the Rutherford Appleton Laboratory.

### References

- Albrecht BA, Bretherton CS, Johnson D, Schubert WH, Frisch AS. 1995. The Atlantic Stratocumulus Transition Experiment – ASTEX. *Bull. Am. Meteorol. Soc.* **76**: 889–904.
- Bougeault P, André J-C. 1986. On the stability of the third-order turbulence closure for the modeling of the stratocumulus-topped boundary layer. *J. Atmos. Sci.* **43**: 1574–1581.
- Bozier KE, Pearson GN, Collier CG. 2007. Doppler lidar observations of Russian forest fire plumes over Helsinki. *Weather* **62**: 203–208.
- Carson DJ. 1973. The development of a dry inversion-capped convectively unstable boundary layer. *Q. J. R. Meteorol. Soc.* **99**: 450–467.
- Davies F, Collier CG, Pearson GN, Bozier KE. 2004. Doppler lidar measurements of turbulent structure function over an urban area. *J. Atmos. Oceanic Technol.* **21**: 753–761.
- Davies F, Middleton DR, Bozier KE. 2007. Urban air pollution modelling and measurements of boundary-layer height. *Atmos. Environ.* **41**: 4040–4049.
- Davis KJ, Gamage N, Hagelberg CR, Kiemle C, Lenschow DH, Sullivan PP. 2000. An objective method for deriving atmospheric structure from airbourne lidar observations. *J. Atmos. Oceanic Technol.* **17**: 1455–1468.
- Garratt JR. 1992. *The atmospheric boundary layer*. Cambridge Univ. Press: Cambridge, UK.
- Grant ALM. 1997. An observational study of the evening transition boundary layer. *Q. J. R. Meteorol. Soc.* **123**: 657–677.
- Hogan RJ, Gaussiat N, Illingworth AJ. 2005. Stratocumulus liquid water content from dual-wavelength radar. *J. Atmos. Oceanic Technol.* **22**: 1207–1218.
- Hunt JCR, Kaimal JC, Gaynor JE. 1988. Eddy structure in the convective boundary layer – New measurements and new concepts. *Q. J. R. Meteorol. Soc.* **114**: 827–858.
- Illingworth AJ, Hogan RJ, O'Connor EJ, Bouniol D, Brooks ME, Delanoë J, Donovan DP, Eastment JD, Gaussiat N, Goddard JWF, Haeffelin M, Klein Baltink H, Krasnov OA, Pelon J, Piriou J-M, Protat A, Russchenberg HWJ, Seifert A, Tompkins AM, van Zadelhoff GJ, Vinit F, Willén U, Wilson DR, Wrench CL. 2007. Cloudnet – Continuous evaluation of cloud profiles in seven operational models using ground-based observations. *Bull. Am. Meteorol. Soc.* **88**: 883–898.
- LeMone MA. 1990. Some observations of vertical velocity skewness in the convective planetary boundary layer. *J. Atmos. Sci.* **47**: 1163–1169.
- Lenschow DH, Wyngaard JC, Pennell WT. 1980. Mean-field and second-moment budgets in a baroclinic, convective boundary layer. *J. Atmos. Sci.* **37**: 1313–1326.
- Lock AP, Brown AR, Bush MR, Martin GM, Smith RNB. 2000. A new boundary-layer mixing scheme – 1. Scheme description and single-column model tests. *Mon. Weath. Rev.* **128**: 3187–3199.
- Moeng C-H, Rotunno R. 1990. Vertical velocity skewness in the buoyancy-driven boundary layer. *J. Atmos. Sci.* **47**: 1149–1162.
- Moyer KA, Young GS. 1991. Observations of vertical velocity skewness within the marine stratocumulus-topped boundary layer. *J. Atmos. Sci.* **48**: 403–410.
- Nicholls S. 1984. The dynamics of stratocumulus: Aircraft observations and comparisons with a mixed-layer model. *Q. J. R. Meteorol. Soc.* **110**: 783–820.
- Nicholls S. 1989. The structure of radiatively driven convection in stratocumulus. *Q. J. R. Meteorol. Soc.* **112**: 431–460.
- Nicholls S, LeMone MA. 1980. The fair-weather boundary layer in GATE: The relationship of subcloud fluxes and structure to the distribution and enhancement of cumulus clouds. *J. Atmos. Sci.* **37**: 2051–2067.
- O'Connor EJ, Hogan RJ, Illingworth AJ. 2005. Retrieving stratocumulus drizzle parameters using Doppler radar and lidar. *J. Appl. Meteorol.* **44**: 14–27.
- Pearson GN, Davies F, Collier CG. 2009. An analysis of the performance of the UFAM pulsed Doppler lidar for observing the boundary layer. *J. Atmos. Oceanic Technol.* **26**: 240–250.
- Sorbjan Z. 1989. *Structure of the atmospheric boundary layer*. Prentice Hall: New Jersey.
- vanZanten MC, Duynkerke PG, Cuijpers JWM. 1999. Entrainment parameterization in convective boundary layers. *J. Atmos. Sci.* **56**: 813–828.
- Young GS. 1988. Turbulence structure of the convective boundary layer – 1. Variability of normalized turbulence statistics. *J. Atmos. Sci.* **45**: 719–726.